

# Intensification of tilted atmospheric vortices by asymmetric diabatic heating

Tom Dörffel<sup>1</sup>, Ariane Papke<sup>1</sup>, Rupert Klein<sup>1</sup>, Piotr Smolarkiewicz<sup>2</sup>

<sup>1</sup>FB Mathematik & Informatik, Freie Universität Berlin, Berlin, Germany

<sup>2</sup>European Centre for Medium Range Weather Forecasts, Reading, United Kingdom

(Received ?? and in revised form ??)

Päschke et al. (JFM, **701**, 137–170 (2012)) studied the nonlinear dynamics of strongly tilted vortices subject to asymmetric diabatic heating by asymptotic methods. They found, *i.a.*, that an azimuthal Fourier mode 1 heating pattern can intensify or attenuate such a vortex depending on the relative orientation of tilt and heating asymmetries. The theory originally addressed the gradient wind regime which, asymptotically speaking, corresponds to vortex Rossby numbers of order  $\mathcal{O}(1)$  in the limit. Formally, this restricts the applicability of the theory to rather weak vortices in the near equatorial region. It is shown below that said theory is, in contrast, uniformly valid for vanishing Coriolis parameter and thus applicable to vortices up to hurricane strength. The paper's main contribution is a series of three-dimensional numerical simulations which fully support the analytical predictions.

---

## 1. Introduction

Atmospheric vortex intensification and the associated evolution of vortex structure remain a topic of intense investigations. As Smith & Montgomery (2017) point out in their review article, intricate interactions of boundary layer processes, moist thermodynamics, multiscale stochastic deep convection, and the vortex-scale fluid dynamics produce the observed, sometimes extremely rapid intensification of incipient hurricanes. They also emphasize that, despite the valuable insights that have been gained in many studies of idealized axisymmetric flow models, asymmetries of vortex structure, convection patterns, and boundary layer structure have been observed to be important for vortex intensification in real-life situations.

This study focuses on the question of how asymmetric heating in the bulk vortex above the boundary layer can induce sizeable vortex amplification. Following, e.g., Nolan & Montgomery (2002); Nolan & Grasso (2003); Nolan *et al.* (2007) we adopt the point of view that latent heat release from condensation can be modelled, with limitations, by external diabatic heat sources in dry air. In the cited studies, non-axisymmetric heating patterns were shown to have at most a small effect on vortex strength within the framework of linearizations about an axisymmetric upright vortex. These results of linear theory were corroborated in Nolan & Grasso (2003); Nolan *et al.* (2007) by comparison with fully nonlinear three-dimensional simulations.

Investigating incipient hurricanes that develop from easterly waves in the tropical atlantic Dunkerton *et al.* (2009) revealed, however, that such vortices can exhibit very strong tilt. Thus, for instance, the locations of the vortex center at heights equivalent to the 925 hPa and 200 hPa pressure levels are located about 200 km apart in their figure 21. This amounts to an overall vortex tilt at a scale comparable to the vortex

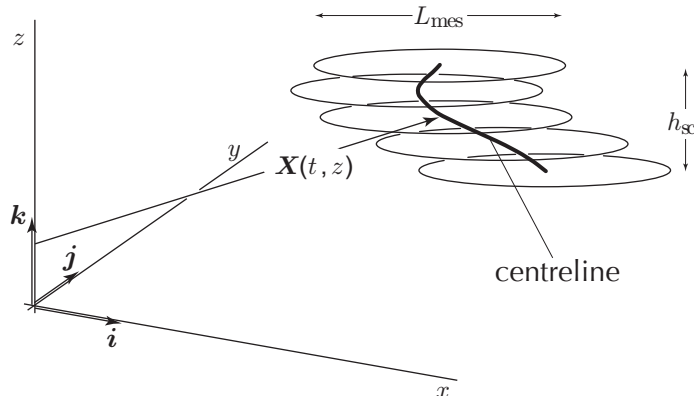


FIGURE 1. Sketch of the spatial scaling regime for vortices in this work. In each horizontal plane the vortex is axisymmetric to leading order while the vortex center line position  $\mathbf{X}(t, z)$  covers horizontal distances comparable to the vortex core size (adapted from Päsche *et al.* (2012)).

diameter, *i.e.*, to a situation that clearly does not allow for linearizations about an upright vortex.

Our study revisits the work of Päsche *et al.* (2012) who analyzed the dynamics of strongly tilted atmospheric vortices in the gradient wind regime by matched asymptotic expansions. They obtained a closed coupled set of evolution equations for the primary circulation structure and the vortex centerline, and demonstrated that in a strongly tilted vortex symmetric and asymmetric heating patterns can have a comparable impact on vortex intensity. As by its very definition the gradient wind regime is restricted to vortex Rossby numbers of order unity, this theory has thus far been considered applicable only to rather weak vortices with intensities far from the interesting stage of the tropical storm/hurricane transition (Montgomery 2017).

To allow for vortices in this transition regime, we consider here the dynamics of meso-scale atmospheric vortices  $L_{\text{mes}} \sim 100$  km that extend vertically across the depth of the troposphere  $h_{\text{sc}} \sim 10$  km but feature large vortex Rossby number  $\text{Ro}_{\text{mes}} \gg 1$ . We use the asymptotic techniques introduced by Päsche *et al.* (2012) and recycle many of their technical steps. As indicated in fig. 1, we assume vortices with nearly axisymmetric core structure at each horizontal level, and we allow for strong vortex tilt such that the vortex centers observed at different heights may be displaced horizontally relative to each other by distances comparable to the vortex core size  $L_{\text{mes}}$ .

One of the main findings of Päsche *et al.* (2012) was the following evolution equation for the primary circulation described by the axisymmetric leading-order circumferential velocity,  $u_\theta$ , valid for time scales large compared to the vortex turnover time scale,

$$\frac{\partial u_\theta}{\partial t} + w_0 \frac{\partial u_\theta}{\partial z} + u_{r,00} \left( \frac{\partial u_\theta}{\partial r} + \frac{u_\theta}{r} + f_0 \right) = -u_{r,*} \left( \frac{u_\theta}{r} + f_0 \right). \quad (1.1)$$

Here  $(t, r, z)$  are the appropriately rescaled time, radial, and vertical coordinates,  $f_0$  is the Coriolis parameter, and  $w_0$  and  $u_{r,00}$  are the axisymmetric components of the vertical and radial velocities induced by *the axisymmetric mean heating patterns*, also properly rescaled. The apparent radial velocity  $u_{r,*}$  results from an interaction of the vortex tilt with the asymmetric first circumferential Fourier mode of the vertical velocity.

In particular,

$$u_{r,*} = \frac{1}{2\pi} \int_{-\pi}^{\pi} w \mathbf{e}_r \cdot \frac{\partial \mathbf{X}}{\partial z} d\theta, \quad (1.2)$$

where  $\mathbf{X}(t, z)$  is the time dependent vortex centerline position at height  $z$  (see fig. 1),  $w$  is the full vertical velocity, and  $\mathbf{e}_r = \mathbf{i} \cos(\theta) + \mathbf{j} \sin(\theta)$  is the radial unit vector of a horizontal polar coordinate system attached to the centerline.

The main findings of the present work are:

(a) The evolution equation from (1.1) is uniformly valid as  $f_0 \rightarrow 0$  so that it holds, in particular, also for  $\text{Ro}_{\text{mes}} \gg 1$ , *i.e.*, for vortices of hurricane strength.

(b) The mechanism of vortex spin-up by asymmetric heating of a tilted vortex is traced back analytically to an effective circumferential mean vertical mass flux divergence that arises when the first Fourier mode diabatic heating and the vortex tilt correlate positively.

(c) Equation (1.1) can be recast into a balance equation for kinetic energy,  $e_k = \rho_0 \frac{u_{\theta}^2}{2}$ ,

$$(re_k)_t + (ru_{r,00} [e_k + \tilde{p}])_r + (rw_0 [e_k + \tilde{p}])_z = \frac{r\rho_0}{N^2\bar{\Theta}^2} [\tilde{\Theta}_0 Q_{\Theta,0} + \tilde{\Theta}_1 \cdot \mathbf{Q}_{\Theta,1}] \quad (1.3)$$

in line with the theory by Lorenz (1955) for available potential energy (APE) generation. Here  $\tilde{p}$  is the relevant pressure perturbation,  $\tilde{\Theta}_0, Q_{\Theta,0}$  are the axisymmetric means of potential temperature perturbations and of the diabatic heating, respectively,  $\tilde{\Theta}_1, \mathbf{Q}_{\Theta,1}$  are dipole vectors whose components are the cosine and sine coefficients of their first circumferential Fourier modes, and  $N$  and  $\bar{\Theta}$  are the Brunt-Visälä frequency and the background potential temperature stratification, respectively. Equation (1.3) states that, except for a conservative redistribution of kinetic energy due to advection and the work of the pressure perturbation,  $p'$ , positive correlations of diabatic sources and potential temperature perturbations generate the potential energy available for increasing the kinetic energy of the vortex.

Nolan *et al.* (2007) study the effects of asymmetric diabatic heating on vortex strength in a linearized model. One of their conclusions is that “... purely asymmetric heating generally leads to vortex weakening, usually in terms of the symmetric energy, and always in terms of the low-level wind.” The present theory shows that this conclusion does not hold up in case of a strongly tilted vortex, but that in this case symmetric and suitably arranged asymmetric heating have vortex intensification efficiencies of the same order of magnitude.

(d) The theory compares favorably with three-dimensional numerical simulations based on the compressible Euler equations.

To arrive at these results, we first recount the governing equations and the principles of our analytical approach in section 2, and then revisit the derivations by Päscheke *et al.* (2012). A discussion of the scaling regime is given in section 3 to investigate the influence of the Coriolis effect (item (a)), and the asymptotic vortex core expansion is carried out in section 4 analytically supporting the physical interpretation of the asymmetric intensification mechanism given in item (b). In section 5 we establish the kinetic energy balance from item (c). Section 6 presents results of the theory in comparison with three-dimensional computational simulations to corroborate item (d). Conclusions and an outlook are provided in section 7.

---

Gravitational acceleration	$g$	=	9.81	$\text{m s}^{-2}$
Coriolis parameter ( $\phi = 30^\circ$ N)	$f_{\text{ref}}$	=	$7.3 \cdot 10^{-5}$	$\text{s}^{-1}$
$(df/dy)_0$ ( $\phi = 30^\circ$ N)	$\beta_{\text{ref}}$	=	$2.0 \cdot 10^{-11}$	$\text{m}^{-1} \text{s}^{-1}$
Pressure	$p_{\text{ref}}$	=	$10^5$	Pa
Temperature	$T_{\text{ref}}$	=	300	K
Brunt-Väisälä frequency	$N_{\text{ref}}$	=	$10^{-2}$	$\text{s}^{-1}$
Dry air gas constant	$R$	=	287	$\text{m s}^{-2} \text{K}^{-1}$
Isentropic exponent	$\gamma$	=	1.4	

---

TABLE 1. Characteristic atmospheric flow parameters

## 2. Dimensionless governing equations and distinguished limits

### 2.1. Governing equations

The dimensionless inviscid rotating compressible flow equations for an ideal gas with constant specific heat capacities in the beta plane approximation used as the basis for the subsequent asymptotic analysis for  $\varepsilon \rightarrow 0$  read (Klein 2010)

$$\frac{\partial \mathbf{u}}{\partial t} + \mathbf{u} \cdot \nabla_{\parallel} \mathbf{u} + w \frac{\partial \mathbf{u}}{\partial z} + \frac{1}{\varepsilon^3} \frac{1}{\rho} \nabla_{\parallel} p + \varepsilon (f + \varepsilon^3 \beta y) \mathbf{k} \times \mathbf{u} = 0, \quad (2.1a)$$

$$\frac{\partial w}{\partial t} + \mathbf{u} \cdot \nabla_{\parallel} w + w \frac{\partial w}{\partial z} + \frac{1}{\varepsilon^3} \frac{1}{\rho} \frac{\partial p}{\partial z} = -\frac{1}{\varepsilon^3}, \quad (2.1b)$$

$$\frac{\partial \rho}{\partial t} + \mathbf{u} \cdot \nabla_{\parallel} \rho + w \frac{\partial \rho}{\partial z} + \rho \nabla_{\parallel} \cdot \mathbf{u} + \rho \frac{\partial w}{\partial z} = 0, \quad (2.1c)$$

$$\frac{\partial \Theta}{\partial t} + \mathbf{u} \cdot \nabla_{\parallel} \Theta + w \frac{\partial \Theta}{\partial z} = Q_{\Theta}, \quad (2.1d)$$

$$\Theta = \frac{p_{\text{ref}}}{\rho R} \left( \frac{p}{p_{\text{ref}}} \right)^{\frac{1}{\gamma}}. \quad (2.1e)$$

Here  $p, \rho, \Theta, \mathbf{u}, w$  are pressure, density, potential temperature, and the horizontal and vertical velocities, and  $\gamma$  is the specific heat ratio. The Coriolis parameters  $f$  and  $\beta$  are constants of order unity. The three-dimensional gradient is  $\nabla = \nabla_{\parallel} + \mathbf{k} \partial/\partial z$  with the horizontal gradient  $\nabla_{\parallel} = \mathbf{i} \partial/\partial x + \mathbf{j} \partial/\partial y$ , the zonal, meridional, and vertical coordinates  $(x, y, z)$ , and the related unit vectors  $(\mathbf{i}, \mathbf{j}, \mathbf{k})$ . Finally,  $t$  is the time variable and  $Q_{\Theta}$  is a diabatic source term. The meaning of the small parameter  $\varepsilon$  will be explained shortly.

Table 1 lists general characteristics of the near-tropical atmosphere combined in Table 2 to form reference values for non-dimensionalization. Let an asterisk denote dimensional quantities, then the unknowns and coordinates in (2.1) are

$$p = \frac{p^*}{p_{\text{ref}}}, \quad \rho = \frac{\rho^*}{\rho_{\text{ref}}}, \quad (\mathbf{u}, w) = \frac{(\mathbf{u}^*, w^*)}{u_{\text{ref}}}, \quad (\mathbf{x}, z) = \frac{(\mathbf{x}^*, z^*)}{h_{\text{sc}}}, \quad t = \frac{t^* u_{\text{ref}}}{h_{\text{sc}}}. \quad (2.2)$$

Note that  $u_{\text{ref}}$  is an estimate of the large-scale thermal wind shear, and  $\mathbf{x} = ix + jy$ .

In deriving the dimensionless equations (2.1) using the quantities from tables 1, 2 the Mach, internal wave Froude, and Rossby numbers, and the  $\beta$ -parameter

$$\begin{aligned} \text{M} &= \frac{u_{\text{ref}}}{\sqrt{RT_{\text{ref}}}} \approx 3.4 \cdot 10^{-2} & \text{Ro} &= \frac{u_{\text{ref}}}{f_{\text{ref}} h_{\text{sc}}} \approx 13.3 \\ \text{Fr} &= \frac{u_{\text{ref}}}{N_{\text{ref}} h_{\text{sc}}} \approx 1.1 \cdot 10^{-1} & \hat{\beta} &= \frac{\beta_{\text{ref}} h_{\text{sc}}}{f_{\text{ref}}} \approx 2.7 \cdot 10^{-3} \end{aligned} \quad (2.3)$$

emerge naturally. These are replaced with functions of a single small expansion parameter

---

Density	$\rho_{\text{ref}} = \frac{p_{\text{ref}}}{RT_{\text{ref}}} \sim 1.16 \text{ kg m}^{-3}$
Potential temperature	$\Delta\Theta = T_{\text{ref}} \frac{h_{\text{sc}} N_{\text{ref}}^2}{g} \sim 40 \text{ K}$
Velocity	$u_{\text{ref}} = \frac{\tan\phi}{\pi/2} \frac{N_{\text{ref}}^2}{f_{\text{ref}}^2} \beta h_{\text{sc}}^2 \sim 10 \text{ m s}^{-1}$
Length	$h_{\text{sc}} = \frac{p_{\text{ref}}}{g\rho_{\text{ref}}} \sim 8.8 \text{ km}$
Time	$t_{\text{ref}} = \frac{h_{\text{sc}}}{u_{\text{ref}}} \sim 10^3 \text{ s}$

---

TABLE 2. Derived reference values for non-dimensionalization

$\varepsilon \ll 1$  through the distinguished limits

$$M = \varepsilon^{3/2}, \quad \text{Fr} = \frac{\varepsilon}{N}, \quad \text{Ro} = \frac{1}{\varepsilon f}, \quad \hat{\beta} = \varepsilon^3 \beta, \quad (2.4)$$

in line with the multiscale asymptotic modelling framework from (Klein 2010). Here  $(N, f, \beta) = \mathcal{O}(1)$  as  $\varepsilon \rightarrow 0$ , with concrete values

$$N = 0.91, \quad f = 0.75, \quad \beta = 2.7 \quad (2.5)$$

derived from (2.3) for  $\varepsilon = M^{2/3} = 0.1$ . Whereas  $f$  and  $\beta$  appear explicitly in (2.1),  $N$  characterizes the background stratification of potential temperature and will be invoked below where we define the initial conditions for the vortex flow.

Equations (2.1) will form the basis for the subsequent asymptotic analysis for  $\varepsilon \ll 1$ , although much of the expansions will proceed in terms of the small parameter

$$\delta = \sqrt{\varepsilon}. \quad (2.6)$$

### 3. Scaling regime for large vortex Rossby number and strong tilt

#### 3.1. Vortex core size, intensity, and evolution time scale

Vortex core sizes of 50 km to 200 km are typical for tropical storms and hurricanes, and the storm/hurricane threshold lies at wind speeds of 30 m/s (Emanuel 2003). With  $\delta^2 \equiv \varepsilon \sim 1/10$ ,  $h_{\text{sc}} \sim 10$  km, and  $u_{\text{ref}} \sim 10$  m/s, these data correspond well with

$$L_v \sim h_{\text{sc}}/\delta^2 \approx 100 \text{ km}, \quad u_{\text{max}} \sim u_{\text{ref}}/\delta \approx 33 \text{ m/s}, \quad \delta p_v \sim \delta^4 p_{\text{ref}}, \quad (3.1)$$

for a characteristic vortex core size  $L_v$ , a typical wind speed, and the associated depression in the vortex core, respectively. Note that these scalings deviate from those adopted by Päsche *et al.* (2012), who considered systematically larger radii of the order  $L_v \sim h_{\text{sc}}/\delta^3$  needed for direct matching to a quasi-geostrophic large scale outer flow. From their work we recall, however, that the vortex core structure and tilt develop on a time scale  $t_v$  that is by  $1/\delta^2$  longer than the vortex core turnover time scale  $t_{\text{to}} = L_v/u_{\text{max}}$ . Thus, in view of (3.1), we will follow the vortex core evolution on the time scale

$$t_v = \frac{t_{\text{to}}}{\delta^2} = \frac{1}{\delta^2} \frac{h_{\text{sc}}}{\delta^2} \frac{\delta}{u_{\text{ref}}} = \frac{t_{\text{ref}}}{\delta^3} \sim 10 \text{ h}. \quad (3.2)$$

The scalings in (3.1) and (3.2) include the regime of “rapid intensification”, defined by NOAA’s National Hurricane Center (<http://www.nhc.noaa.gov/aboutgloss.shtml>) to denote maximum wind accelerations of 30 kt  $\sim 15$  m/s in 24h.

Also, the adopted scalings describe a vortex in the cyclostrophic regime since

$$\frac{h_{\text{sc}}}{u_{\text{ref}}^2} \frac{u_{\theta}^2}{r} = \mathcal{O}(1) \quad \text{whereas} \quad \frac{h_{\text{sc}}}{u_{\text{ref}}^2} f_{\text{ref}} u_{\theta} = \frac{1}{\text{Ro}} \frac{u}{u_{\text{ref}}} = \mathcal{O}(\delta), \quad (3.3)$$

*i.e.*, the Coriolis term is subordinate to the centripetal acceleration in the horizontal momentum balance in this regime. Accordingly, the vortex Rossby number is large,

$$\text{Ro}_v = \frac{u_{\text{max}}}{f_0 L_v} = \text{Ro} \frac{u_{\text{max}}}{u_{\text{ref}}} \frac{h_{\text{sc}}}{L_v} = \mathcal{O}(\delta^{-2-1+2}) = \mathcal{O}\left(\frac{1}{\delta}\right). \quad (3.4)$$

### 3.2. Co-moving coordinates for a strongly tilted vortex

Following Päsche *et al.* (2012), we resolve the flow dynamics on the vortex precession and core evolution time scale  $t_v$  from (3.2). The appropriate time coordinate is

$$\hat{t} = \delta^3 t. \quad (3.5)$$

For the core structure analysis we introduce vortex centered horizontal coordinates

$$\mathbf{x} = \frac{1}{\delta^2} (\mathbf{X}(\hat{t}, z) + \hat{\mathbf{x}}) \quad (3.6)$$

where  $\mathbf{X}(\hat{t}, z)$  is the horizontal position of the vortex centerline at height  $z$  and  $\hat{\mathbf{x}}$  is the relative horizontal offset. With this scaling  $\hat{\mathbf{x}}$  resolves the core scale  $L_v$  from (3.1) and the centerline covers comparable distances. This justifies the notion of “strong tilt”.

In the sequel we use polar coordinates in horizontal planes, *i.e.*,

$$\hat{\mathbf{x}} = \hat{x} \mathbf{i} + \hat{y} \mathbf{j} \quad \text{where} \quad \begin{cases} \hat{x} = \hat{r} \cos \theta; & \mathbf{i} = \mathbf{e}_r \cos \theta - \mathbf{e}_\theta \sin \theta \\ \hat{y} = \hat{r} \sin \theta; & \mathbf{j} = \mathbf{e}_r \sin \theta + \mathbf{e}_\theta \cos \theta \end{cases} \quad (3.7)$$

with  $\mathbf{e}_r$  and  $\mathbf{e}_\theta$  the radial and circumferential unit vectors, respectively. The transformation rules for derivatives in these coordinates read

$$\nabla_{\parallel} = \delta^2 \left( \mathbf{e}_r \frac{\partial}{\partial \hat{r}} + \mathbf{e}_\theta \frac{1}{\hat{r}} \frac{\partial}{\partial \theta} \right) \equiv \delta^2 \hat{\nabla}, \quad (3.8a)$$

$$\frac{\partial}{\partial z} \Big|_{t,x,y} = \frac{\partial}{\partial z} \Big|_{\hat{t},\hat{r},\theta} - \frac{\partial \mathbf{X}}{\partial z} \cdot \hat{\nabla}, \quad (3.8b)$$

$$\frac{\partial}{\partial t} \Big|_{x,y,z} = \delta^3 \left( \frac{\partial}{\partial \hat{t}} \Big|_{\hat{r},\theta,z} - \frac{\partial \mathbf{X}}{\partial \hat{t}} \cdot \hat{\nabla} \right). \quad (3.8c)$$

The horizontal velocity is decomposed into the vortex’ motion plus the relative velocity,

$$\mathbf{u} = \delta \frac{\partial \mathbf{X}}{\partial \hat{t}} + (u_r \mathbf{e}_r + u_\theta \mathbf{e}_\theta). \quad (3.9)$$

For later reference, here are the representation of the centerline in the  $(\mathbf{e}_r, \mathbf{e}_\theta)$  basis,

$$\mathbf{X} = (X \cos \theta + Y \sin \theta) \mathbf{e}_r + (-X \sin \theta + Y \cos \theta) \mathbf{e}_\theta, \quad (3.10)$$

and our notation for the Fourier expansion of functions of the circumferential angle,  $\theta$ ,

$$F(\theta) = F_0 + \sum_n (F_{n1} \cos(n\theta) + F_{n2} \sin(n\theta)). \quad (3.11)$$

Note that we have exchanged the roles of  $F_{n1}$  and  $F_{n2}$  relative to their use in (Päsche *et al.* 2012) as this will streamline some of the physical interpretations given below.

## 3.3. Vortex core expansion scheme

The circumferential velocity is expanded as

$$u_\theta(t, \mathbf{x}, z; \varepsilon) = \delta^{-1} u_\theta^{(0)}(t, \hat{r}, z) + u_\theta^{(1)}(t, \hat{r}, z) + \delta u_\theta^{(2)}(t, \hat{r}, \theta, z) + \mathcal{O}(\delta), \quad (3.12a)$$

$$u_r(t, \mathbf{x}, z; \varepsilon) = \delta u_r^{(2)}(t, \hat{r}, \theta, z) + \mathcal{O}(\delta). \quad (3.12b)$$

*i.e.*, non-axisymmetry relative to the centerline is allowed for from  $\mathcal{O}(\delta u_{\text{ref}})$  upwards. Across the core size length scale,  $L_v$ , such asymmetries induce horizontal divergences of order  $u_r/L_v \sim \delta u_{\text{ref}}/(h_{\text{sc}}/\delta^2) = \delta^3 u_{\text{ref}}/h_{\text{sc}}$ , see (3.1). Since the flow field is anelastic to leading order as derived below, this implies the vertical velocity scaling,

$$w(t, \mathbf{x}, z; \varepsilon) = \delta^3 w^{(0)}(t, \hat{r}, \theta, z) + \mathcal{O}(1). \quad (3.13)$$

Expansions for the thermodynamic variables are anticipated as follows,

$$p = p_0 + \delta^2 p_2 + \delta^4 \left( \hat{p}^{(4)} + \hat{p}_4 \right) + \delta^5 \left( \hat{p}^{(5)} + \hat{p}_5 \right) + \mathcal{O}(\delta^5), \quad (3.14a)$$

$$\rho = \rho_0 + \delta^2 \rho_2 + \delta^4 \left( \hat{\rho}^{(4)} + \hat{\rho}_4 \right) + \delta^5 \left( \hat{\rho}^{(5)} + \hat{\rho}_5 \right) + \mathcal{O}(\delta^5), \quad (3.14b)$$

$$\Theta = \Theta_0 + \delta^2 \Theta_2 + \delta^4 \left( \hat{\Theta}^{(4)} + \hat{\Theta}_4 \right) + \delta^5 \left( \hat{\Theta}^{(5)} + \hat{\Theta}_5 \right) + \mathcal{O}(\delta^5), \quad (3.14c)$$

(for plausibility arguments see Päsche *et al.* 2012, section 4.1.3). In (3.14), the variables  $(p_0, p_2, \rho_0, \rho_2, \Theta_0, \Theta_2)(z)$  describe the stationary background,  $(\hat{p}_i, \hat{\rho}_i, \hat{\Theta}_i)(\hat{t}, z)$ , are higher-order horizontal means, and  $(\hat{p}^{(i)}, \hat{\rho}^{(i)}, \hat{\Theta}^{(i)})(\hat{t}, \hat{r}, \theta, z)$  are the quantities of prime interest.

Note that, owing to the Fourier representation defined in (3.11) this notational convention “overloads” the subscript  $(\cdot)_0$  with a double-meaning, but the distinction should always be clear from the context.

The vortex centerline position is expanded as

$$\mathbf{X} = \mathbf{X}^{(0)} + \delta \mathbf{X}^{(1)} + \mathcal{O}(\delta^2). \quad (3.15)$$

## 4. Asymptotic analysis of the core structure evolution

This section revisits the analysis of Päsche *et al.* (2012) for large vortex Rossby numbers focusing on the evolution equation for the primary circulation.

## 4.1. Asymptotic equation hierarchy for the vortex core

The governing equations transformed to the co-moving coordinates are provided in App. A. Inserting the expansion scheme from the previous section we obtain

$$-\frac{(u_\theta^{(0)})^2}{\hat{r}} + \frac{1}{\rho_0} \frac{\partial \hat{p}^{(4)}}{\partial \hat{r}} = 0, \quad \frac{\partial \hat{p}^{(4)}}{\partial \theta} = 0 \quad (4.1a)$$

$$-\frac{2u_\theta^{(0)}u_\theta^{(1)}}{\hat{r}} + \frac{1}{\rho_0} \frac{\partial \hat{p}^{(5)}}{\partial \hat{r}} - f_0 u_\theta^{(0)} = 0, \quad \frac{\partial \hat{p}^{(5)}}{\partial \theta} = 0 \quad (4.1b)$$

from the horizontal momentum balance at leading and first order, respectively. Each line in (4.1) displays the respective radial balance first and the circumferential balance as the second equation. We observe from the radial component in (4.1a) that the vortex is in cyclostrophic balance to leading order which implies large vortex Rossby number. The Coriolis effect enters as a first-order perturbation only in the present regime as seen in the radial component of (4.1b). The pressure perturbations  $p^{(4)}, p^{(5)}$  inherit the assumed

axisymmetry of  $u_\theta^{(0)}, u_\theta^{(1)}$  thanks to the leading and first order circumferential momentum balances in (4.1a) and (4.1b), respectively.

The full second order horizontal momentum equations are listed in appendix B, eqs. (B 1), but for the rest of the paper we only need the circumferential average of the circumferential component (B 1b). Letting  $\psi_0 \equiv \frac{1}{2\pi} \int_{-\pi}^{\pi} \psi(\theta) d\theta$  denote the circumferential average of some  $\theta$ -dependent variable  $\psi$  in line with (3.11), we have

$$\frac{\partial u_\theta^{(0)}}{\partial t} + w_0^{(0)} \frac{\partial u_\theta^{(0)}}{\partial z} + u_{r,0}^{(2)} \left( \frac{\partial u_\theta^{(0)}}{\partial \hat{r}} + \frac{u_\theta^{(0)}}{\hat{r}} \right) - u_{r,*}^{(2)} \frac{\partial u_\theta^{(0)}}{\partial \hat{r}} = 0, \quad (4.2)$$

where

$$u_{r,*}^{(2)} = \left( w^{(0)} \mathbf{e}_r \cdot \frac{\partial \mathbf{X}^{(0)}}{\partial z} \right)_0. \quad (4.3)$$

The flow is hydrostatic up to third order, *i.e.*,  $\frac{\partial p_i}{\partial z} = -\rho_i$  ( $i = 1, \dots, 4$ ), whereas

$$\frac{\partial \hat{p}^{(4)}}{\partial z} - \frac{\partial \mathbf{X}^{(0)}}{\partial z} \cdot \mathbf{e}_r \frac{\partial \hat{p}^{(4)}}{\partial \hat{r}} = -\hat{\rho}^{(4)}. \quad (4.4)$$

The leading and first order velocities are horizontal and axisymmetric according to (3.12), (3.13) and thus divergence free. The second order velocity is subject to an anelastic divergence constraint obtained from the mass balance,

$$\frac{\rho_0}{\hat{r}} \left( \frac{\partial}{\partial \hat{r}} (\hat{r} u_r^{(2)}) + \frac{\partial u_\theta^{(2)}}{\partial \theta} \right) + \frac{\partial}{\partial z} (\rho_0 w^{(0)}) - \frac{\partial \mathbf{X}^{(0)}}{\partial z} \cdot \hat{\nabla}_\parallel (\rho_0 w^{(0)}) = 0. \quad (4.5)$$

Similarly, the first non-trivial potential temperature transport equation reads

$$\frac{u_\theta^{(0)}}{\hat{r}} \frac{\partial \hat{\Theta}^{(4)}}{\partial \theta} + w^{(0)} \frac{d\Theta_1}{dz} = Q_\Theta^{(0)}, \quad (4.6)$$

and the equation of state relates the thermodynamic perturbation variables through

$$\hat{\rho}^{(4)} = \rho_0 \left( \frac{\hat{p}^{(4)}}{\gamma p_0} - \frac{\hat{\Theta}^{(4)}}{\Theta_0} \right). \quad (4.7)$$

#### 4.2. Temporal evolution of the vortex structure

Päschke *et al.* (2012) observe that with the aid of (4.1) and (4.3)–(4.7), and given the vortex tilt,  $\partial \mathbf{X}^{(0)}/\partial z$ , as well as the diabatic source term,  $Q_\Theta^{(0)}$ , one may interpret (4.2) as a closed evolution equation for the leading order circumferential velocity,  $u_\theta^{(0)}$ .

To corroborate this, we use the Fourier decomposition, (3.11), for  $w^{(0)}$  and the representation of the centerline representation in polar coordinates from (3.10) to obtain

$$u_{r,*}^{(2)} = \left( w^{(0)} \mathbf{e}_r \cdot \frac{\partial \mathbf{X}^{(0)}}{\partial z} \right)_0 = \frac{1}{2} \left[ w_{11}^{(0)} \frac{\partial X^{(0)}}{\partial z} + w_{12}^{(0)} \frac{\partial Y^{(0)}}{\partial z} \right]. \quad (4.8)$$

Expressions for  $w_0^{(0)}$  and  $w_{1k}^{(0)}$  for  $k = 1, 2$  follow from the  $\Theta$ -transport equation in (4.6),

$$w_0^{(0)} \frac{d\Theta_1}{dz} = Q_{\Theta,0}^{(0)}, \quad w_{1k}^{(0)} \frac{d\Theta_1}{dz} = Q_{\Theta,1k}^{(0)} - (-1)^k \frac{u_\theta^{(0)}}{\hat{r}} \hat{\Theta}_{1[3-k]}^{(4)}. \quad (4.9)$$

Since  $\hat{p}^{(4)}$  is axisymmetric (see (4.1a)),  $\hat{p}_{1k}^{(4)} \equiv 0$  and the equation of state, (4.7), yields



$\widehat{\Theta}_{1k}^{(4)}/\Theta_0 = -\widehat{\rho}_{1k}^{(4)}/\rho_0$ . With this information, the vertical momentum balance (4.4) yields

$$\frac{\widehat{\Theta}_{11}^{(4)}}{\Theta_0} = -\frac{\widehat{\rho}_{11}^{(4)}}{\rho_0} = -\frac{1}{\rho_0} \frac{\partial X^{(1)}}{\partial z} \frac{\partial \widehat{p}^{(4)}}{\partial \widehat{r}}, \quad \frac{\widehat{\Theta}_{12}^{(4)}}{\Theta_0} = -\frac{\widehat{\rho}_{12}^{(4)}}{\rho_0} = -\frac{1}{\rho_0} \frac{\partial Y^{(1)}}{\partial z} \frac{\partial \widehat{p}^{(4)}}{\partial \widehat{r}}. \quad (4.10)$$

Using the gradient wind balance in (4.1a) to eliminate  $\partial \widehat{p}^{(4)}/\partial \widehat{r}$ , and going back to (4.9) we obtain explicit expressions for the  $w_{1k}^{(0)}$  in terms of  $u_\theta^{(0)}$ ,  $\partial \mathbf{X}^{(0)}/\partial z$ , and  $Q_\Theta^{(0)}$ ,

$$w_{1k}^{(0)} \frac{d\Theta_1}{dz} = Q_{\Theta,1k}^{(0)} + (-1)^k \Theta_0 \frac{\partial X_{[3-k]}^{(0)}}{\partial z} \frac{(u_\theta^{(0)})^3}{\widehat{r}^2} \quad (k = 1, 2), \quad (4.11)$$

where  $X_1^{(0)} \equiv X^{(0)}$  and  $X_2^{(0)} \equiv Y^{(0)}$ . Upon insertion of this result in (4.8), the second term on the right cancels, so that

$$u_{r,*}^{(2)} = \frac{1}{2 d\Theta_1/dz} \left[ Q_{\Theta,11}^{(0)} \frac{\partial X^{(0)}}{\partial z} + Q_{\Theta,12}^{(0)} \frac{\partial Y^{(0)}}{\partial z} \right] \equiv \frac{1}{2 d\Theta_1/dz} \mathbf{Q}_{\Theta,1} \cdot \frac{\partial \mathbf{X}}{\partial z}. \quad (4.12)$$

Here we have interpreted the cosine and sine Fourier components of  $Q_\Theta^{(0)}$  as the components of a heating dipole vector,  $\mathbf{Q}_\Theta$ , in the horizontal plane.

To find a corresponding expression for  $u_{r,0}^{(2)}$  (see the third term in (4.2)), consider the circumferential average of mass continuity, (4.5). A brief calculation yields

$$\frac{\partial (\widehat{r} \rho_0 u_{r,0}^{(2)})}{\partial \widehat{r}} + \frac{\partial (\widehat{r} \rho_0 w_0^{(0)})}{\partial z} - \frac{1}{2} \left[ \frac{\partial X^{(1)}}{\partial z} \frac{\partial (\widehat{r} \rho_0 w_{11}^{(0)})}{\partial \widehat{r}} + \frac{\partial Y^{(1)}}{\partial z} \frac{\partial (\widehat{r} \rho_0 w_{12}^{(0)})}{\partial \widehat{r}} \right] = 0 \quad (4.13)$$

or, equivalently,

$$\frac{\partial (\widehat{r} \rho_0 [u_{r,0}^{(2)} - u_{r,*}^{(2)}])}{\partial \widehat{r}} + \frac{\partial (\widehat{r} \rho_0 w_0^{(0)})}{\partial z} = 0 \quad (4.14)$$

with  $u_{r,*}^{(2)}$  defined in (4.8). Exploiting (4.11) in that definition and integrating in  $\widehat{r}$  requiring that  $u_{r,0}^{(2)}$  be finite at  $\widehat{r} = 0$  we find

$$u_{r,0}^{(2)} = u_{r,00}^{(2)} + u_{r,*}^{(2)}, \quad (4.15)$$

where

$$u_{r,00}^{(2)} = -\frac{1}{\widehat{r}} \int_0^{\widehat{r}} \frac{r}{\rho_0} \frac{\partial}{\partial z} \left( \rho_0 \frac{Q_{\Theta,0}^{(0)}}{d\Theta_1/dz} \right) dr. \quad (4.16)$$

With (4.9) (first equation), (4.12), (4.15), and (4.16) we have now indeed expressed  $w_0^{(0)}$ ,  $u_{r,0}^{(2)}$ , and  $u_{r,*}^{(2)}$  in terms of  $u_\theta^{(0)}$ ,  $\partial \mathbf{X}/\partial z$ , and  $Q_\Theta^{(0)}$  as announced. In the sequel, we may thus derive from (4.2) how vortex tilt and diabatic heating affect the evolution of the primary circulation.

The results in this section match the corresponding result by Päsche *et al.* (2012) with the Coriolis parameter  $f_0$  set to zero. This corroborates our statement (a) in the introduction that the vortex amplification/attenuation mechanism described in their work does not depend on the vortex Rossby number being at most of order unity.

## 5. Discussion of the intensification/attenuation mechanism

### 5.1. The influence of asymmetric heating on the primary circulation

As elaborated in the previous section, (4.2) describes the evolution of the primary circulation in response to external diabatic heating in the present vortex flow regime. Aiming

[htbp]

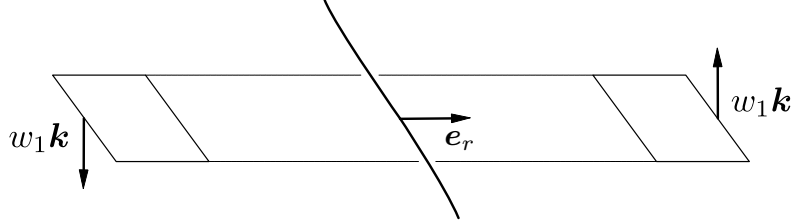


FIGURE 2. Origin of the effective vertical mass flux divergence induced by Fourier mode 1 vertical velocity perturbations with amplitude  $w_1$  in a tilted vortex when the  $w_1$ -dipole and vortex tilt are suitably correlated.

to separate the influence of heating asymmetries from those of axisymmetric effects, we recall from (4.15) that the net circumferentially averaged radial velocity is entirely a response to diabatic effects, and that it consists of one part,  $u_{r,00}^{(2)}$ , which, according to (4.16) is induced by axisymmetric heating, and a second part,  $u_{r,*}^{(2)}$ , which, according to (4.12), arises from first Fourier mode asymmetric heating patterns. Using this decomposition in (4.2), we rewrite the equation as

$$\frac{\partial u_\theta^{(0)}}{\partial t} + w_0^{(0)} \frac{\partial u_\theta^{(0)}}{\partial z} + u_{r,00}^{(2)} \left( \frac{\partial u_\theta^{(0)}}{\partial \hat{r}} + \frac{u_\theta^{(0)}}{\hat{r}} \right) = -u_{r,*}^{(2)} \frac{u_\theta^{(0)}}{\hat{r}}, \quad (5.1)$$

which is the version of the equation announced in (1.1) in the introduction. In this equation, the left hand side captures the influence of the axisymmetric dynamics and diabatic heating, whereas the right hand side covers all effects due to the interaction of asymmetric heating and vortex tilt.

### 5.2. Mechanics of vortex intensification by asymmetric heating of a tilted vortex

In a preliminary step we analyze the two versions of the leading-order mass balance in (4.13) and (4.14). The term in square brackets in (4.13) results from application of the transformation rule for the vertical derivative in (3.8) to the vertical mass flux divergence,  $w\rho_z + \rho w_z = (\rho w)_z$ , in the continuity equation (2.1c). Figure 2 reveals the origin of the term: Consider the toroidal control volume defined by radial and vertical intervals  $(r, r + \Delta r)$  and  $(z, z + \Delta z)$ , in the centerline-attached coordinate system as shown in the figure. A Fourier mode 1 vertical velocity mode, when suitably arranged relative to the vortex tilt, will produce a net outflow from the control volume across the tilted cylindrical outer interface as indicated by the up and downward pointing arrows in the graph. As this consideration concerns the  $r = \text{const.}$ -part of the control volume interface, this flux contributes the apparent radial flux associated with  $u_{r,*}^{(2)}$  in the mass balance from (4.14).

Note, however, that the true mass motion associated with this term is *vertical* as explained above. As a consequence, considering the effect of mass motions on the angular momentum budget in the form of (4.2), this apparent radial flux does not come with the usual spin-up / spin-down that is otherwise associated with radial motions due to the conservation of angular momentum as encoded in the term  $u_{r,0}^{(2)} u_\theta^{(0)} / \hat{r}$ .

This should settle the announcement of (item *b*) in the introduction.

## 5.3. Energy budget for the externally heated vortex

Here we elaborate on how the asymmetric diabatic heating is transferred to kinetic energy of the primary circulation in a tilted vortex. To this end, we multiply (5.1) by  $\rho_0 \hat{r} u_\theta^{(0)}$ , use the  $\theta$ -averaged leading-order mass balance from (4.14) and recast the advective terms in conservation form to obtain,

$$\frac{\partial}{\partial t} \left( \hat{r} \rho_0 \frac{u_\theta^2}{2} \right) + \frac{\partial}{\partial \hat{r}} \left( \hat{r} \rho_0 u_{r,00}^{(2)} \frac{u_\theta^2}{2} \right) + \frac{\partial}{\partial z} \left( \hat{r} \rho_0 w_0 \frac{u_\theta^2}{2} \right) = -\hat{r} u_{r,0}^{(2)} \frac{\partial p^{(4)}}{\partial \hat{r}}. \quad (5.2)$$

Here we have dropped the  $(0)$  superscript on  $u_\theta^{(0)}$  and  $w_0^{(0)}$  to simplify the notation, and we have used the cyclostrophic radial momentum balance from (4.1) to introduce the pressure gradient on the right.

This reveals the change of kinetic energy (left hand side) to result from the work of the pressure force due to the mean radial motion (right hand side). Some straightforward but lengthy calculations, the details of which are given in appendix C, yield a direct relation of the kinetic energy balance in (5.2) to the Lorenz' theory of generation of available potential energy (APE) by diabatic heating,

$$(\hat{r} e_k)_t + \left( \hat{r} u_{r,00}^{(2)} h_k \right)_{\hat{r}} + \left( \hat{r} w_0^{(0)} h_k \right)_z = \frac{\hat{r} \rho_0}{d\Theta_1/dz} \frac{1}{\Theta_0} \left[ \Theta_0^{(4)} Q_{\Theta,0}^{(0)} + \Theta_1^{(4)} \cdot \mathbf{Q}_{\Theta,1}^{(0)} \right], \quad (5.3)$$

where  $h_k = e_k + p^{(4)}$ , and  $(\Theta, \mathbf{Q}_\Theta)_1 = (\Theta, Q_\Theta)_{12} \mathbf{i} + (\Theta, Q_\Theta)_{11} \mathbf{j}$  are the dipole vectors spanned by the first circumferential Fourier components of the fourth order potential temperature perturbation,  $\Theta^{(4)}$ , and of the diabatic heating function,  $Q_\Theta^{(0)}$ , respectively. This result shows, in line with Lorenz (1955, 1967) and as announced in the introduction in (1.3), how positively correlated heat addition and temperature perturbations generate available potential energy (APE), which is then redistributed by the advective and pressure-velocity fluxes as seen on the right of (5.3). The precise form of the right hand side of (1.3) as announced in the introduction (item *c*) is obtained from (5.3) by realizing that  $(1/\Theta_0)d\Theta_1/dz$  is the dimensionless representation of  $N^2$ , the square of the Brunt-Väisälä frequency, and that the constant  $\Theta_0$  is the leading-order dimensionless background potential temperature  $\bar{\Theta} = T_{\text{ref}}(\Theta_0 + o(1))$ .

Nolan *et al.* (2007), extending prior similar studies, investigate the influence of asymmetric diabatic heating on vortex intensification on the basis of a linearized anelastic model that includes a radially varying base state and baroclinic primary circulation. Their central conclusions are that (i) asymmetric heating patterns quite generally tend to attenuate a vortex, that (ii) there are situations in which they can induce amplification, but in these cases, their influence is (iii) generally rather weak. In fact, they state in their section e: "... purely asymmetric heating generally leads to vortex weakening, usually in terms of the symmetric energy, and always in terms of the low-level wind.". Equation (5.3) shows that purely asymmetric heating in a tilted vortex can intensify or attenuate a vortex depending on the arrangement of the heating pattern relative to the tilt, and that the efficiencies of symmetric and asymmetric heating in generating kinetic energy are of the same order in the asymptotics as claimed in item *c* of the introduction.

## 6. Comparison with 3D numerical simulations

The following section presents the setup and results of 3D numerical simulations. We want to corroborate the outlined theory, especially the relation of tilt, asymmetric heating and the evolution of the centerline by numerical solutions of the Euler equations. For this kind of atmospheric problem, the use of a numerical framework is necessary suit-

able for the forward-in-time integration of the equations of fluid dynamics constrained to a (nearly) steady background state. Conveniently, EULAG (see, *e.g.*, Prusa *et al.* 2008) offers the necessary features and its compressible model was used during all the simulations outlined in the following section.

Subsection 6.1 gives an outline of the numerical setup, especially of the initial data and subsection 6.2 presents the different numerical tests corroborating our theory and discusses the results.

### 6.1. Numerical settings and initial data

Along the lines of Papke (2017), the simulation domain extends 4000 km in the horizontal direction and 10 km in the vertical. Time integration length is of the order of days for all simulations and the CFL number is initially chosen to be approximately 0.15, but changes due to a constant time step size and varying velocity. Boundary conditions are set to solid-wall conditions and a damping layer surrounds the domain near the horizontal boundaries to suppress unwanted gravity waves due to imbalances of the initial data. The background stratification is set with respect to the constant Brunt-Väisälä frequency and reference values (corresponding to  $z = 0$ ) of pressure, temperature, and density given in tables 1 and 2. In particular, the background stratification of potential temperature is given by

$$\bar{\Theta}(z) = T_{\text{ref}} \exp\left(\frac{N_{\text{ref}}^2}{g} z\right). \quad (6.1)$$

Emphasizing the cyclostrophic regime the asymptotic scale analysis carried out in section 4, the Coriolis parameter for our simulations is set to zero.

Päschke *et al.* (2012) worked out in subsection 6.2. that a cosine-shaped centerline is an eigenmode of the centerline equations of motion for exponential background density distribution, constant Brunt-Väisälä frequency, and under the Boussinesq approximation. For this reason the initial centerline is set to

$$\mathbf{X}(z) = \mathbf{n} \cos(\pi z / z_{\text{top}}), \quad \text{where } \mathbf{n} = (80, 80)^T \text{ km} \quad (6.2)$$

for all simulations.

Based on recent studies (Papke 2017, and references therein) the initial velocity distribution follows a Gaussian profile of the  $z$ -component of the vorticity:

$$q(r) = q_m e^{-\sigma^2 r^2} \quad (6.3)$$

This results in a radial profile of circumferential velocity of the form

$$u_\theta = q_m \frac{1 - e^{-\sigma^2 r^2}}{2\sigma^2 r}. \quad (6.4)$$

Such a profile features typical characteristics of the circumferential velocity of a tropical cyclone, *i.e.*, a linear increase in the inner regions, a ring of maximum wind, and a decay for large radii of order  $\mathcal{O}(r^{-1})$ . A qualitative depiction is given in fig. 3.

From the constraints  $\partial_r u_\theta|_{r=R_{\text{mw}}} = 0$  and  $u_\theta|_{r=R_{\text{mw}}} = u_{\theta, \text{max}}$  we get

$$q_m = \frac{u_{\theta, \text{max}}}{R_{\text{mw}}} e^{\sigma^2 R_{\text{mw}}^2} \quad (6.5)$$

with  $\sigma R_{\text{mw}} \approx 1.12$ .  $R_{\text{mw}}$  and  $u_{\theta, \text{max}}$  denote the radius of maximum wind and the maximum wind speed and are canonically chosen to  $R_{\text{mw}} = 100$  km and  $u_{\theta, \text{max}} = 10$  m/s.

For compliance with the boundary conditions a mollifier is applied, reducing the ve-

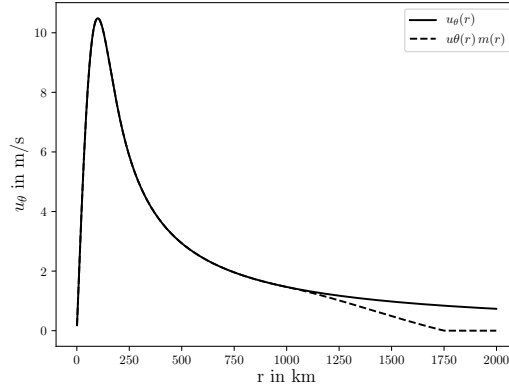


FIGURE 3. Radial circumferential velocity profile corresponding to a Gaussian profile of vertical vorticity. The solid line corresponds to the unmodified profile (6.4) and the dashed line to the actual profile after applying the mollifier, see eq. (6.6).

locity to zero at large radii:

$$u_\theta = q_m \frac{1 - e^{-\sigma^2 r^2}}{2\sigma^2 r} m(r) \quad (6.6)$$

with

$$m(r) = \begin{cases} 1 & , \quad r < r_0 \\ \cos^2\left(\frac{\pi}{2} \frac{r-r_0}{\rho_0-r_\infty}\right) & , \quad r_0 < r < r_\infty \\ 0 & , \quad r > r_\infty \end{cases} \quad (6.7)$$

$r_0 = 1\,250$  km and  $r_\infty = 1\,750$  km are the radii where the mollifier starts and where it reaches full-suppression.

The asymptotic theory of section 4 raises several constraints of leading and next-to-leading-order horizontal structure for pressure, potential temperature and vertical velocity. The pressure is determined by the vertical hydrostatic background distribution at leading order and corrected by the cyclostrophic balance at  $\mathcal{O}(\delta^4)$ . With a prescribed radial profile of circumferential velocity we can solve (4.1a) by using QUADPACK's `qag` routine (cf. Favati *et al.* 1991) with boundary values  $\partial_r p|_{r=0} = (p - \bar{p})|_{r>r_\infty} = 0$ .

Due to tilt and hydrostatic balance the cyclostrophic pressure perturbation imprints a perturbation on the potential temperature, see (4.10). Having the pressure perturbation and its derivative with the hydrostatic balance  $\hat{p}^{(4)}$  we can compute the density correction and with the equation of state (4.7) the perturbation  $\hat{\Theta}^{(4)}$ . However, using (4.10) to set the horizontally non-homogeneous part of  $\Theta$  leads to significantly better initial balancing.

To be in initial balance with the diabatic heating we have to compute the vertical velocity from equations (4.9) and (4.11). The next subsection will give more details for the different types of heating.

## 6.2. Results and discussion

Different aspects of the theory developed by Päscheke *et al.* (2012) and extended in this paper are tested via numerical simulations.

A starting point is the initially tilted vortex without diabatic heating. In this setting  $u_{r,*}^{(2)}$ ,  $u_{r,00}^{(2)}$ , and  $w_0^{(0)}$  vanish (see (4.16), (4.8), and (4.9)), reducing (5.1) to

$$\frac{\partial}{\partial t} u_\theta^{(0)} = 0. \quad (6.8)$$

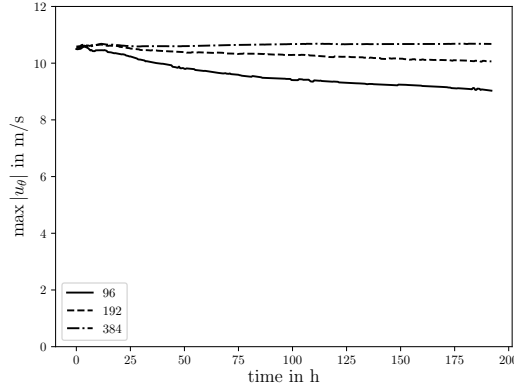


FIGURE 4. Time series of tangential velocity for different resolutions and without diabatic heating. The lines correspond to  $96^2 \times 20$  (solid),  $192^2 \times 20$  (dashed), and  $384^2 \times 40$  (dash-dotted) grid points.

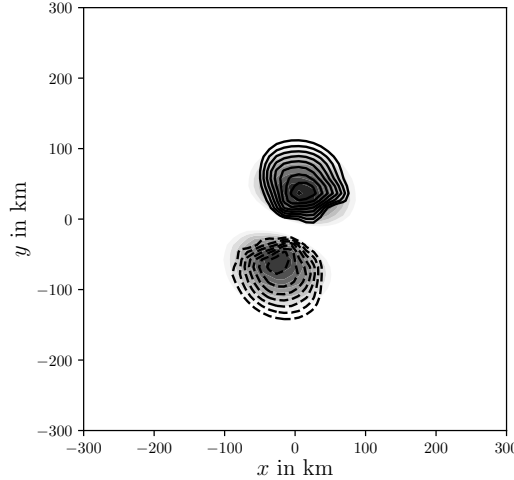


FIGURE 5. Typical pattern of vertical velocity for a horizontal slice. Contours depict the numerical results at 5000 m high and  $t = 36$  h with absolute values ranging from 0.02 m/s to 0.05 m/s in step of 0.005 m/s with positive (solid lines) and negative (dashed lines) sign. Underlying shades represent the theoretical prediction.

Additionally, (4.11) implies that without external heating only the tilt imprints a dipol pattern on  $w^{(0)}$ :

$$w^{(0)} = \frac{\Theta_0}{d\Theta_1/dz} \left( \sin \theta \frac{\partial X^{(1)}}{\partial z} - \cos \theta \frac{\partial Y^{(1)}}{\partial z} \right) \frac{(u_\theta^{(0)})^3}{\hat{r}^2} \quad (k = 1, 2) \quad (6.9)$$

We performed this test for different resolutions and checked for several error estimates. Figure 4 presents the time evolution of the maximum value of the angle-averaged circumferential velocity. This result is in line with (6.8) showing reasonably constant wind speed, although resolution dependent-damping occurs. We conclude that the highest presented resolution gives sufficient results for this test and thus, we use it for the following benchmarks.

Figure 5 shows the comparison of theoretically predicted vertical velocity (shaded) and the actual results from the simulations (contours). Qualitatively there is a good congruence of theoretical and numerical values. In terms of absolute values both quantities

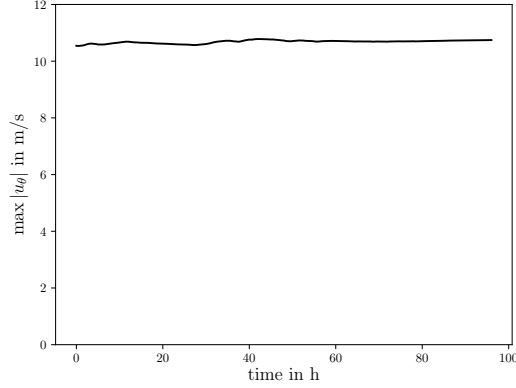


FIGURE 6. Time series of maximum wind for the heating pattern (6.10). As predicted by the theory no significant impact on the horizontal velocity occurs.

deviate with an order of  $\mathcal{O}(\delta)$ .  $w^{(0)}$  ranges from  $\sim -0.6$  m/s to  $\sim 0.6$  m/s while the numerical values are in  $\sim -0.45$  m/s to  $\sim 0.45$  m/s. This might be due to the excitation of an additional asymptotic expansion mode due to slight imbalances of the initial data and calls for more detailed investigation in the near future.

Taking again equation (4.11) into consideration and restricting to asymmetric (dipole) heating patterns we find an arrangement for which  $w^{(0)}$  must be suppressed. This can be accomplished by

$$Q_{\Theta,1k}^{(0),*} = (-1)^{k+1} \Theta_0 \frac{\partial X_{[3-k]}^{(1)}}{\partial z} \frac{(u_{\theta}^{(0)})^3}{\widehat{r}^2} \quad (k = 1, 2), \quad (6.10)$$

*i.e.*, a heating dipole rotated  $-\pi/2$  relative to the tilt. This setup also leads to  $u_{r,*}^{(2)} = 0$  and therefore no impact on the circumferential velocity is expected.

The numerical experiments have shown that the application of (6.10) leads to strong numerical instabilities on a very fast timescale and, as being imposed on purely mathematical consideration, it might be too strong anyway. A second justification for this approach is the fact that, although analytically balanced, the initial data might not be balanced from a numerical point of view. Indeed, we initially observe fast equilibrations, which decay within a few hours. For the actual numerical simulation we found that it is convenient to use a time-dependent *blending function*. It is constructed from three freely specifiable points  $(t_i, f_i)$ ,  $i = 0, 1, 2$ , and linear interpolation in between:

$$f(t) = \begin{cases} 0 & , \quad t < t_0 \\ f_0 + \frac{f_1 - f_0}{t_1 - t_0} (t - t_0) & , \quad t_0 \leq t < t_1 \\ f_1 + \frac{f_2 - f_1}{t_2 - t_1} (t - t_1) & , \quad t_1 \leq t < t_2 \\ & , \quad t \geq t_2 \end{cases} \quad (6.11)$$

We now have the possibility to let the system equilibrate before applying the diabatic heating. For this experiment we chose  $(t_i, f_i) \in \{(12 \text{ h}, 0), (24 \text{ h}, 1), (36 \text{ h}, 0)\}$ .

As predicted fig. 7 shows that the resulting vertical velocity can be suppressed by a factor of  $\delta$ , effectively canceling  $w^{(0)}$ . The remaining contributions to  $w$  might be due to excited higher-order modes of the asymptotic expansion. Furthermore the impact on the angle-averaged circumferential velocity is negligible, see fig. 6.

In general, we find that the resulting vertical velocity is composed of a tilt-induced

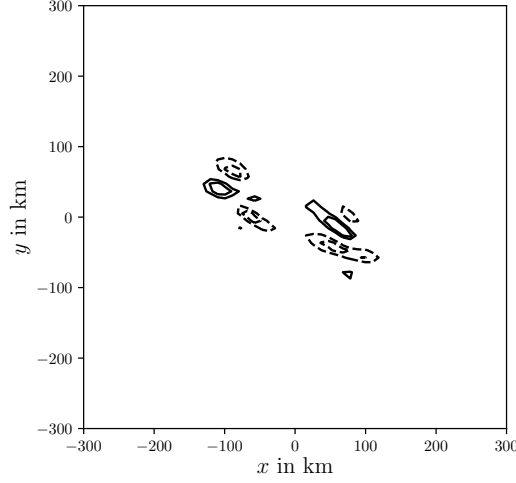


FIGURE 7. Residual vertical velocity the the heating pattern (6.10). Contours represent 0.01 m/s and 0.02 m/s with positive (solid lines) and negative (dashed lines) sign.

part and another one induced by the diabatic heating. We recall from (4.11) that

$$\mathbf{w}_1^{(0)} = \frac{\mathbf{Q}_{\Theta,1}^{(0)}}{d\Theta_1/dz} + \frac{\Theta_0}{d\Theta_1/dz} \mathbf{R}_{-\pi/2} \frac{\partial \mathbf{X}^{(1)}}{\partial z} \frac{(u_\theta^{(0)})^3}{\hat{r}^2}, \quad (6.12)$$

where  $\mathbf{R}_{\theta_0}$  is the conventional twodimensional rotation matrix for the angle  $\theta_0$ .

The goal of this paper is to show that the proposed mechanism can be used to trigger vortex amplification by asymmetric diabatic heating. (5.1) and (4.12) let us conclude that the maximum intensification can be achieved by a heating pattern antiparallel to the tilt and maximum attenuation by parallel alignment.

Taking the heating pattern (6.10) we can generalize

$$\mathbf{Q}_{\Theta,1}^{(2)} = \mathbf{R}_{\theta_0} \Theta_0 \frac{\partial \mathbf{X}^{(1)}}{\partial z} \frac{(u_\theta^{(0)})^3}{\hat{r}^2}, \quad (6.13)$$

and we find maximum amplification for  $\theta_0 = -\pi$ . In addition the vertical velocity results in

$$\mathbf{w}_1^{(0)} = \sqrt{2} \mathbf{R}_{-5\pi/4} \frac{\Theta_0}{d\Theta_1/dz} \frac{\partial \mathbf{X}^{(1)}}{\partial z} \frac{(u_\theta^{(0)})^3}{\hat{r}^2}. \quad (6.14)$$

The first intensification test was performed using the heating pattern (6.13) without any modifications. We see a strong increase in horizontal average wind speed in fig. 8 and a good correlation between theory and simulation for  $w$  in fig. 9. Nonetheless, it has shown that this “prototypical” heating pattern leads to very strong distortions of all physical fields and finally to a non-physical behaviour of the solution.

Therefore, the next test was performed in a slightly different fashion to weaken the effect of diabatic heating. As the evolution equation for  $u_\theta^{(0)}$  and the default heating would exhibit a singularity for  $u_\theta^{(0)}$  at finite time ( $\partial_t u_\theta^{(0)} \propto (u_\theta^{(0)})^4$ ) we decided to calculate  $Q_\Theta$  using the initial distribution  $u_\theta(t=0)$  instead of  $u_\theta(t)$ . The application of the blending function also appeared to be useful. Parameters are set to  $(t_i, f_i) \in \{(12 \text{ h}, 0), (24 \text{ h}, 1), (36 \text{ h}, 0)\}$ .

We are now not able to directly compare numerical and analytical values of  $w$  anymore. This is for three reasons: (i) As previously shown imbalances of the initial data are causing



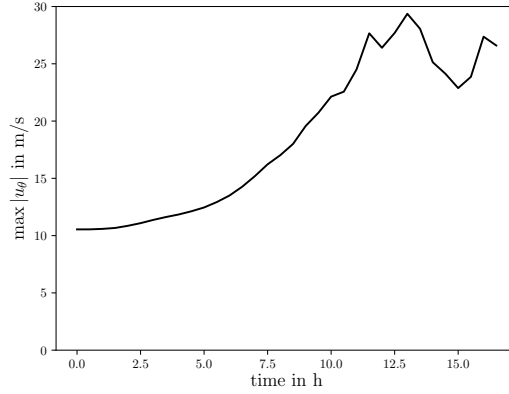


FIGURE 8. Time series of increased maximum wind due to diabatic heating (6.13).

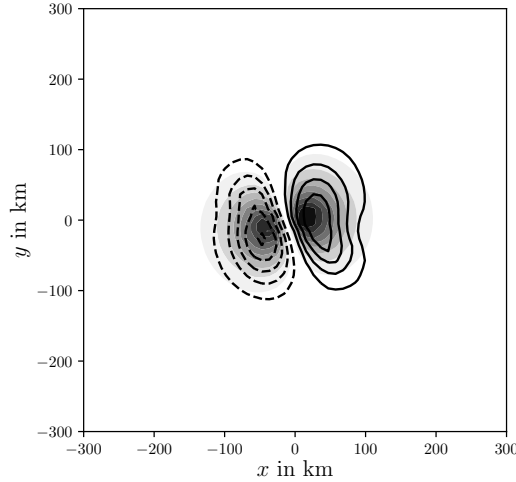


FIGURE 9. Contours depict the numerical results for vertical velocity at 5000 m high and  $t = 5$  h with absolute values ranging from 0.02 m/s to 0.04 m/s in step of 0.004 m/s with positive (solid lines) and negative (dashed lines) sign. Underlying shades represent the theoretical prediction.

the excitation of higher-order modes of  $w^{(i)}$ . (ii) In calculating the heating pattern  $u_{\theta}$  is replaced by its initial distribution. (iii) The blending of  $Q_{\theta}$  via (6.11) continuously alters the rotation angle between  $\mathbf{w}_1^{(0)}$  and  $\partial_z \mathbf{X}^{(1)}$  from  $-\pi/2$  to  $-5\pi/4$  and back. This is due to the varying ratio between tilt-induced and diabatically induced vertical velocity. Nonetheless, fig. 10 depicting the vertical velocity at maximum heating still shows good congruence between theory and simulation.

Moreover, we are able to intensify the maximum wind speed from 10.5 m/s to  $\sim 17.5$  m/s by applying the bespoke heating pattern, see fig. 11. After  $t = 36$  h the vortex runs freely to show that the intensification sustains without heating after horizontal redistribution of angular momentum. Interestingly, although the heating begins at  $t = 12$  h a sudden increase starts to happen at  $t \approx 24$  h. On the one hand, this reflects the nonlinear character of the intensification mechanism. On the other hand, this complies very well with observations, where sudden strong intensifications are observed.

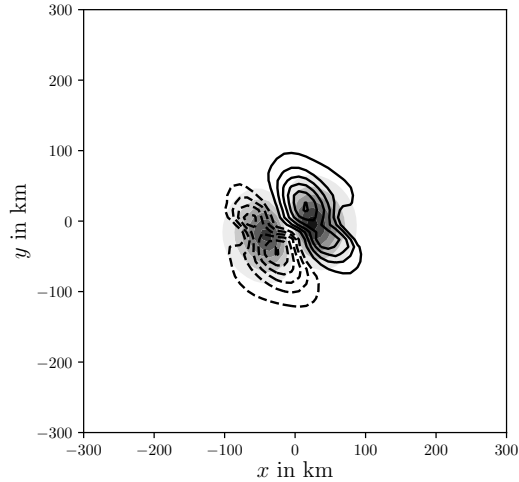


FIGURE 10. Vertical velocity resulting from diabatic heating (6.13) with applied blending function. For details see fig. 9.

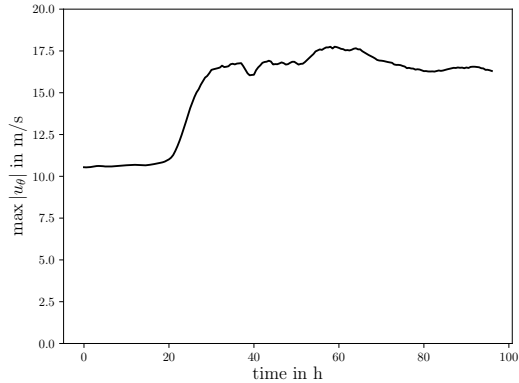


FIGURE 11. Time series of increased maximum wind due to diabatic heating (6.13) with applied blending function. The heating acts between  $t = 12$  h and  $t = 36$  h with its peak at  $t = 24$  h. The strong increase sustains after the heating was switched off.

## 7. Conclusions and outlook

With the present work we have extended the results of Päsche *et al.* (2012) to large vortex Rossby numbers, and we have corroborated their theoretical prediction of rather strong intensification efficiencies of asymmetric diabatic heating in a strongly tilted vortex through numerical simulations.

Ongoing work concerns the self-consistent modelling of heating patterns in the form of latent heat release from multiscale moist processes, and a consistent coupling to the dynamics of the near-surface boundary layer.

T.D., A.P., and R.K. thank Deutsche Forschungsgemeinschaft for their support through Grant CRC 1114 “Scaling Cascades in Complex Systems”, project C06 “Multi-scale structure of atmospheric vortices” and the Helmholtz Society of Research Institutions for funding through the “GeoSim” Graduate College.

### Appendix A. Governing equations in the co-moving coordinates

Transforming (2.1) to the vortex-centered coordinates from section 3.2 using (3.8) and defining  $\mathbf{U} \equiv \delta \partial \mathbf{X} / \partial t$  and  $\mathbf{u}_{\text{rel}} = u_r \mathbf{e}_r + u_\theta \mathbf{e}_\theta$  we find

$$\begin{aligned} \frac{\partial(\mathbf{U} + \mathbf{u}_{\text{rel}})}{\partial \hat{t}} + \frac{1}{\delta} \mathbf{u}_{\text{rel}} \cdot \widehat{\nabla} \mathbf{u}_{\text{rel}} + \frac{w}{\delta^3} \left[ \frac{\partial}{\partial z} - \frac{\partial \mathbf{X}}{\partial z} \cdot \widehat{\nabla} \right] (\mathbf{U} + \mathbf{u}_{\text{rel}}) \\ + \frac{1}{\delta^7} \frac{1}{\rho} \widehat{\nabla} p + \frac{1}{\delta^2} f \mathbf{k} \times (\mathbf{U} + \mathbf{u}_{\text{rel}}) = 0, \end{aligned} \quad (\text{A } 1a)$$

$$\begin{aligned} \frac{\partial w}{\partial \hat{t}} + \frac{1}{\delta} \mathbf{u}_{\text{rel}} \cdot \widehat{\nabla} w + \frac{w}{\delta^3} \left[ \frac{\partial}{\partial z} - \frac{\partial \mathbf{X}}{\partial z} \cdot \widehat{\nabla} \right] w \\ + \frac{1}{\delta^{10}} \left( \frac{1}{\rho} \left[ \frac{\partial}{\partial z} - \frac{\partial \mathbf{X}}{\partial z} \cdot \widehat{\nabla} \right] p + 1 \right) = 0, \end{aligned} \quad (\text{A } 1b)$$

$$\frac{\partial \rho}{\partial \hat{t}} + \frac{1}{\delta} \widehat{\nabla} \cdot (\rho \mathbf{u}_{\text{rel}}) + \frac{1}{\delta^3} \left[ \frac{\partial}{\partial z} - \frac{\partial \mathbf{X}}{\partial z} \cdot \widehat{\nabla} \right] (\rho w) = 0, \quad (\text{A } 1c)$$

$$\frac{\partial \Theta}{\partial \hat{t}} + \frac{1}{\delta} \mathbf{u}_{\text{rel}} \cdot \widehat{\nabla} \Theta + \frac{w}{\delta^3} \left[ \frac{\partial}{\partial z} - \frac{\partial \mathbf{X}}{\partial z} \cdot \widehat{\nabla} \right] \Theta = Q_\Theta. \quad (\text{A } 1d)$$

### Appendix B. Full second order horizontal momentum balances

$$\begin{aligned} \frac{u_\theta^{(0)}}{\hat{r}} \frac{\partial u_r^{(2)}}{\partial \theta} - \frac{2u_\theta^{(0)} u_\theta^{(2)}}{\hat{r}} - \frac{(u_\theta^{(1)})^2}{\hat{r}} + \mathbf{e}_\theta \cdot \frac{\partial \mathbf{X}^{(0)}}{\partial z} \frac{w^{(0)} u_\theta^{(0)}}{\hat{r}} \\ + \frac{1}{\rho_0} \frac{\partial \widehat{p}^{(6)}}{\partial \hat{r}} - \frac{\rho_1}{\rho_0^2} \frac{\partial \widehat{p}^{(4)}}{\partial \hat{r}} - f_0 u_\theta^{(1)} = 0 \end{aligned} \quad (\text{B } 1a)$$

$$\begin{aligned} \frac{\partial u_\theta^{(0)}}{\partial t} + w^{(0)} \frac{\partial u_\theta^{(0)}}{\partial z} + u_r^{(2)} \left( \frac{\partial u_\theta^{(0)}}{\partial \hat{r}} + \frac{u_\theta^{(0)}}{\hat{r}} \right) + \frac{u_\theta^{(0)}}{\hat{r}} \frac{\partial u_\theta^{(2)}}{\partial \theta} \\ - w^{(0)} \mathbf{e}_r \cdot \frac{\partial \mathbf{X}^{(0)}}{\partial z} \frac{\partial u_\theta^{(0)}}{\partial \hat{r}} + \frac{1}{\rho_0 \hat{r}} \frac{\partial \widehat{p}^{(6)}}{\partial \theta} = 0 \end{aligned} \quad (\text{B } 1b)$$

### Appendix C. Derivation of the kinetic energy budget (5.3)

We start from (5.1), which is equivalent to (4.21) in (Päschke *et al.* 2012) for  $f_0 = 0$ . This is verified straightforwardly by using  $u_{r,0}^{(2)} = u_{r,00}^{(2)} + u_{r,*}^{(2)}$ . The equation is multiplied by  $\hat{r} \rho_0 u_\theta^{(0)}$ , and we use the mass conservation law in the form of eq. (4.14), *i.e.*,

$$\left( \hat{r} \rho_0 u_{r,00}^{(2)} \right)_{\hat{r}} + \left( \hat{r} \rho_0 w_0^{(0)} \right)_z = 0, \quad (\text{C } 1)$$

to generate the advective transport terms of kinetic energy in conservation form. We let

$$e_k = \rho_0 u_\theta^{(0)2} / 2 \quad (\text{C } 2)$$

and obtain

$$\left( \hat{r} e_k \right)_t + \left( \hat{r} u_{r,00}^{(2)} e_k \right)_{\hat{r}} + \left( \hat{r} w_0^{(0)} e_k \right)_z = -\hat{r} \left( u_{r,00}^{(2)} + u_{r,*}^{(2)} \right) \frac{\partial p^{(4)}}{\partial \hat{r}}. \quad (\text{C } 3)$$

Focusing on the left hand side of this equation, we rewrite the first term as

$$\begin{aligned} \widehat{r}u_{r,00}^{(2)} \frac{\partial p^{(4)}}{\partial \widehat{r}} &= \left( \widehat{r}u_{r,00}^{(2)} p^{(4)} \right)_{\widehat{r}} + \left( \widehat{r}w_0^{(0)} p^{(4)} \right)_z - \widehat{r}\rho_0 w_0^{(0)} \left( \frac{p^{(4)}}{\rho_0} \right)_z \\ &\quad - \frac{p^{(4)}}{\rho_0} \left[ \left( \widehat{r}\rho_0 u_{r,00}^{(2)} \right)_{\widehat{r}} + \left( \widehat{r}\rho_0 w_0^{(0)} \right)_{\widehat{r}} \right]. \end{aligned} \quad (\text{C } 4)$$

The square bracket vanishes according to (C 1), while we observe that by combining the axisymmetric part of the hydrostatic balance in (4.4) with the equation of state in (4.7) to replace  $(p^{(4)}/\rho_0)_z$ , and (cr) to replace  $w_0^{(0)}$  one finds

$$\widehat{r}\rho_0 w_0^{(0)} \left( \frac{p^{(4)}}{\rho_0} \right)_z = \widehat{r}\rho_0 \frac{Q_{\Theta,0}^{(0)}}{d\Theta_1/dz} \frac{\widehat{\Theta}_0^{(4)}}{\Theta_0}. \quad (\text{C } 5)$$

Next we rewrite the second term on the right of (C 3) using the definition of  $u_{r,*}^{(2)}$  in (4.8), and the first Fourier modes of the vertical momentum balance in (4.10) to find

$$\widehat{r}u_{r,*}^{(2)} \frac{\partial p^{(4)}}{\partial \widehat{r}} = \widehat{r}\rho_0 \mathbf{w}_1 \cdot \frac{\Theta_1^{(4)}}{\Theta_0} = \widehat{r}\rho_0 \frac{Q_{\Theta,1}^{(0)}}{d\Theta_1/dz} \cdot \frac{\Theta_1^{(4)}}{\Theta_0}. \quad (\text{C } 6)$$

To obtain the second equality we have used the asymmetric WTG-law from (4.11) and the fact that the second term in that equation contributes a component to  $\mathbf{w}_1$  that is orthogonal  $\partial \mathbf{X}^{(0)}/\partial z$ , and thus also orthogonal to  $\Theta_1^{(4)}$ .

Insertion of (C 4)–(C 6) generates the desired equation (5.3).

## Appendix D. The centerline equation of motion

For the present situation of vanishing background velocity and weak Coriolis effect, the leading order centerline equation of motion reads, dropping the  $^{(0)}$  superscripts for simplicity of notation,

$$\frac{\partial \mathbf{X}}{\partial t} = \mathbf{k} \times \Psi, \quad (\text{D } 1)$$

where

$$\Psi = L_u [\mathcal{H} + \mathcal{I} + \mathcal{J}], \quad (\text{D } 2)$$

and for  $\mathcal{K} \in \{\mathcal{H}, \mathcal{I}, \mathcal{J}\}$

$$L_u [\mathcal{K}] = \lim_{\widehat{r} \rightarrow \infty} \left[ \frac{u}{\widehat{r}} \int_0^{\widehat{r}} \frac{1}{ru^2(r)} \int_0^r r' \mathcal{K}(r') dr' dr \right] = \frac{\pi}{\Gamma} \int_0^\infty r \mathcal{K}(r) dr \quad (\text{D } 3)$$

for a primary circulation  $u(r)$  of total circulation  $\Gamma(z)$ . The  $\mathcal{K}$  are dipole vectors representing first circumferential Fourier modes as introduced above, *i.e.*,

$$\mathcal{K} = \mathcal{K}_{11} \mathbf{i} + \mathcal{K}_{12} \mathbf{j} \quad (\text{D } 4)$$

and their respective definitions are

$$\mathcal{H} = \frac{\partial}{\partial \hat{r}} \left( \hat{r} \mathbf{w}^{(0)} \frac{\partial u_\theta^{(0)}}{\partial z} \right), \quad (\text{D } 5a)$$

$$\mathcal{I} = -\hat{r} \frac{\zeta^{(0)}}{\rho_0} \frac{\partial(\rho_0 \mathbf{w}^{(0)})}{\partial z}, \quad (\text{D } 5b)$$

$$\mathcal{J} = \frac{\partial \phi^{(2)}}{\partial \hat{r}} \left( \hat{r} \frac{\partial \zeta^{(0)}}{\partial \hat{r}} \right), \quad (\text{D } 5c)$$

Here we have introduced the leading-order vorticity

$$\zeta^{(0)} = \frac{\partial u_\theta^{(0)}}{\partial \hat{r}} + \frac{u_\theta^{(0)}}{\hat{r}}, \quad (\text{D } 6)$$

the second order horizontal perturbation velocity potential  $\phi^{(2)}$  responsible for compliance of the solution with mass conservation for purely asymmetric heating,

$$\phi^{(2)} = \hat{r} \int_{\hat{r}}^{\infty} \frac{1}{\bar{r}^3} \left[ \int_0^{\bar{r}} \frac{r^2}{\rho_0} \frac{\partial}{\partial z} (\rho_0 \mathbf{w}^{(0)}) dr \right] d\bar{r}, \quad (\text{D } 7)$$

See also (Päschke *et al.* 2012).

To reveal more clearly the structure of the centerline evolution equation, we recall the formula (4.11) for the vertical velocity Fourier modes, which separates diabatic from adiabatic effects. Rewriting this formula in the dipole vector notation we have

$$\mathbf{w}^{(0)} = \mathbf{w}^Q + \mathbf{w}^{\text{ad}} = \frac{1}{\Theta_1} \left( \mathbf{Q} + U^{(0)} \frac{\partial \mathbf{X}^\perp}{\partial z} \right) \quad \text{with} \quad U^{(0)} = \Theta_0 \frac{(u_\theta^{(0)})^3}{\hat{r}^2}. \quad (\text{D } 8)$$

For the purposes of some idealized tests we decompose the diabatic heating into two separate terms,

$$\mathbf{Q}(\hat{r}, z) = \tilde{\mathbf{Q}}(\hat{r}, z) + \mathbf{Q}(\hat{r}, z) \mathbf{R}_\varphi \frac{\partial \mathbf{X}}{\partial z}(z) \quad (\text{D } 9)$$

where  $\mathbf{R}_\varphi$  denotes the matrix of two-dimensional rotation by an angle  $\varphi$ .

## REFERENCES

- DUNKERTON, T. J., MONTGOMERY, M. T. & WANG, Z. 2009 Tropical cyclogenesis in a tropical wave critical layer: easterly waves. *Atmos. Chem. Phys.* **9**, 5587–5646.
- EMANUEL, K. A. 2003 Tropical cyclones. *Annu. Rev. Earth Planet. Sci.* **31**, 75–104.
- FAVATI, PAOLA, LOTTI, GRAZIA & ROMANI, FRANCESCO 1991 Algorithm 691: Improving quad-pack automatic integration routines. *ACM Trans. Math. Softw.* **17** (2), 218–232.
- KLEIN, R. 2010 Scale-Dependent Asymptotic Models for Atmospheric Flows. *Ann. Rev. Fluid Mech.* **42**, 249–274.
- LORENZ, E. N. 1955 Generation of available potential energy and the intensity of the general circulation. *Tech. Rep.*. UCLA.
- LORENZ, E. N. 1967 The nature and theory of the general circulation of the atmosphere, parts i-iii. TP115 218. World Meteorological Organization.
- MONTGOMERY, M. T. 2017 Private communication.
- NOLAN, D. S. & GRASSO, L. D. 2003 Nonhydrostatic, three-dimensional perturbations to balanced, hurricane-like vortices. Part ii: Symmetric response and nonlinear simulations. *J. Atmos. Sci.* **60** (22), 2717–2745.

- NOLAN, D. S. & MONTGOMERY, M. T. 2002 Nonhydrostatic, three-dimensional perturbations to balanced, hurricane-like vortices. Part i: Linearized formulation, stability, and evolution. *J. Atmos. Sci.* **59** (21), 2989–3020.
- NOLAN, D. S., MOON, Y. & STERN, D. P. 2007 Tropical cyclone intensification from asymmetric convection: Energetics and efficiency. *J. Atmos. Sci.* **64**, 3377–3405.
- PAPKE, A. 2017 Atmospheric vortex stability under vertical shear. PhD thesis, Freie Universität Berlin.
- PÄSCHKE, E., MARSCHALIK, P., OWINOH, A. & KLEIN, R. 2012 Motion and structure of atmospheric mesoscale baroclinic vortices: dry air and weak environmental shear. *J. Fluid Mech.* **701**, 137–170.
- PRUSA, J.M., SMOLARKIEWICZ, P.K. & WYSZOGRODZKI, A.A. 2008 EULAG, a computational model for multiscale flows. *Comput. Fluids* **37**, 1193–1207.
- SMITH, R. K. & MONTGOMERY, M. T. 2017 Recent developments in the fluid dynamics of tropical cyclones. *Ann. Rev. Fluid Mech.* **49**, 1–32.